Modelling determinants of region-specific dopamine dynamics in the striatum

Aske L. Ejdrup[1, †], Jakob K. Dreyer[2], Matthew D. Lycas[1], Søren H. Jørgensen[1], Trevor W. Robbins[3,4], Jeffrey W. Dalley[3,4,5], Freja Herborg[1, †, *], Ulrik Gether[1, †, *]

[1]Department of Neuroscience, Faculty of Health and Medical Sciences, Maersk Tower 7.5, University of Copenhagen, DK-2200 Copenhagen, Denmark

[2]Department of Bioinformatics, H Lundbeck A/S, Valby, Denmark

[3]Behavioural and Clinical Neuroscience Institute, University of Cambridge, Cambridge CB2 3EB, UK

[4]Department of Psychology, University of Cambridge, Cambridge CB2 3EB

[5]Department of Psychiatry, University of Cambridge, Cambridge CB2 0SZ, UK

* These authors contributed equally to the work

† To whom correspondence should be addressed: ejdrup@sund.ku.dk, frejahh@sund.ku.dk or gether@sund.ku.dk

Abstract

Striatal dopamine (DA) release regulates reward-related learning, motivation, and behavioural activation, and is believed to consist of a short-lived *phasic* and continuous *tonic* component. Here, we build a large-scale three-dimensional model of extracellular DA dynamics in the dorsal (DS) and ventral striatum (VS) based on experimentally determined biological parameters. The model predicts rapid dynamics in DS with little-to-no basal DA, whereas lower uptake capacity in VS slows signalling and enables build-up of a *tonic* DA level. Receptor binding simulations reveal that DA D1 receptor occupancy follows extracellular DA concentration with millisecond delay, while DA D2 receptors integrate DA signal over seconds. The modelling further predicts that VS extracellular levels are highly sensitive to DA transporter (DAT) uptake capacity and posit prevalent nanoclustering of DAT in VS as a regulator of DA uptake. Our simulations substantiate regional differences in extracellular DA dynamics and challenge prevailing paradigms of striatal DA signalling.

Introduction

Striatal dopamine (DA) release is essential for regulating reward-related learning, incentive motivation, and motor function[1,2]. DA exerts these roles over a broad range of time scales, yet DA primarily operates as a volume transmitter that targets metabotropic receptors located within a micrometre range from the sites of release[3–7]. The temporal and spatial dynamics of DA release in striatum, however, remain a highly contested topic. Classically, DA release has been divided into *tonic* release, driven by pacemaker-like spontaneous firing, and *phasic* release from coordinated bursts of firing across neurons[5,8,9]. However, this sharp distinction in release modes, as well as the existence of a basal DA level has recently been challenged[1,10–13].

The picture is further complicated by major regional differences across striatal sub domains. These include differences in Ca^{2+}-channel and nicotinic acetylcholine receptor (nAChR) expression profiles on DA terminals, as well differential regulation and expression of the DA transporter (DAT)[14–18]. In addition, we and others have found remarkable differences in extracellular DA release dynamics between the dorsal (DS) and ventral striatum (VS)[12,19,20]. Fibre photometry recordings in the DS in mice using the DA sensor dLight1.3b during self-paced exploratory activity showed a rapidly fluctuating signal, whereas we observed up to minutes-long DA dynamics in VS that correlated with behavioural output[12]. Concurrent measurements of extracellular DA by microdialysis and fibre photometry have furthermore corroborated the lack of tonic levels of DA in DS while supported its presence in VS[12 13]. Despite these reported differences in striatal DA dynamics, electrophysiological recordings suggest that DA neurons from the primary innervators of DS, substantia nigra par compacta (SNc) and VS, ventral tegmental area (VTA), have remarkably similar firing patterns at rest[21]. We therefore set out to better understand the fundamental

principles governing extracellular DA dynamics by constructing a new computational model of the striatal DA system.

Extracellular DA dynamics have been modelled before; either one-dimensionally or with a primary focus on single release events or post-synaptic receptor binding[22–27]. Here, we present a three-dimensional model of tens of thousands of release sites, focused on larger-scale signalling and based on experimentally observed biological parameters. The model faithfully replicates experimentally observed results as well as the difference in DA dynamics between DS and VS. Importantly, it offers compelling evidence that these differences do not primarily reflect different release phenomena but rather arise from differential expression and possibly nanoscale localization of the DA transporter (DAT).

Results

Construction of a model of DA dynamics in the striatum

We constructed a novel model of DA release using experimentally determined parameters from DS, including release, uptake, and cytoarchitecture[5,10,22,23,28,29]. DA release sites on axons projecting from the midbrain were randomly simulated as uniformly distributed discrete points in a three-dimensional space (Fig. 1a). The release events themselves were simulated as point source events[4] driven by action potentials (AP). We then modelled DA release for each voxel in the simulation containing a release site as function of three key parameters; firing rate, release probability and quantal size:

(1)

$$\mathrm{release}_{n,t} = \mathrm{Poisson}(f_{rate}\,dt)_n\, P(R_{\%})_t\, Q\, dt$$

where $\mathrm{Poisson}(f_{rate}\,dt)_n$ is a Poisson distribution of action potentials (AP) for the given neuron (n) with the firing rate f_{rate}[23], $P(R_{\%})_t$ is the probability of release at the individual terminal (t) for each AP, while Q is the number of DA molecules released per event (dopaminergic quantal size) and dt the time step. Changing f_{rate} can be used to model both pacemaker firing, typically reported at 2-10 Hz, and burst firing, which can exceed 20 Hz[5].

DA reuptake in the striatum is almost exclusively mediated by the DA transporter (DAT)[30], which is widely distributed along DA axons and varicosities[31–33]. As reuptake follows concentration-dependent Michaelis-Menten kinetics[34], we simulated uptake as follows:

(2)

$$\text{uptake} = \frac{V_{max}\ [DA]}{K_m\ +\ [DA]}\ dt$$

where [DA] is the concentration of DA for each voxel in the model, V_{max} is the maximal uptake capacity in the region and K_m is the concentration of DA at which half of V_{max} is reached.

The spatial distribution of released DA is a complex interplay between release, uptake and diffusion. Diffusion in an open 3D space can be simulated for each voxel with a Laplacian operator:

(3)

$$\text{diffusion} = \frac{\partial DA_{x,y,z,t}}{\partial t} = D_a\ dt\left(\frac{\partial^2 DA_{x,y,z,t}}{\partial x^2} + \frac{\partial^2 DA_{x,y,z,t}}{\partial y^2} + \frac{\partial^2 DA_{x,y,z,t}}{\partial z^2}\right)$$

where D_a is a corrected diffusion coefficient and *dt* is the timestep. As the extracellular space of the striatum is tortuous, we modified the conventional diffusion coefficient *D* to an apparent diffusion coefficient (D_a) to correct for the tortuosity (λ) of the striatum[4,35]:

(4)

$$D_a = \frac{D}{\lambda^2}$$

Combining equation 1 through 4, we model DA changes in each voxel with a single conceptual equation:

(5)

$$\frac{dDA}{dt} = \text{release} - \text{uptake} + \text{diffusion}$$

We first compared our 3D model of DA dynamics to the analytical solution of a single release event[3,4]. To do this, we simulated a quantal event of 3000 DA molecules and calculated DA concentrations across space at three separate time points (Fig. 1b, c). The analytic solution and our model predicted almost identical results. Slight differences were

116 introduced as the analytical solution assumes linear uptake from DAT while our model
117 incorporate non-linear Michaelis-Menten kinetics. These differences, however, were almost
118 negligible. The main difference between the two models lies in scalability across both space
119 and time. Summarized, the model enables a dynamic incorporation of the surrounding DA
120 concentration, release events and uptake, and can be scaled to cover DA dynamics of a large
121 3D space, whose size and granularity is only limited by computing power (see Code
122 Availability Section for the Python code with numerical implementations of the equations
123 listed and scripts to run the simulations and plot the main figures).
124 We also tested the validity of our model, by examining the response to electrical
125 stimulation. Importantly, our model faithfully mirrored DA release seen with fast-scan cyclic
126 voltammetry (FSCV) recordings upon direct stimulation of striatal slices when we corrected
127 for kinetics of the typical FSCV recording setup (Extended Data Fig. 1b, c and discussion in
128 Supplementary Information)[36–39].
129

130 ## Simulating large scale DA dynamics of the dorsal striatum

131 To better understand the extracellular DA dynamics that arise from the balance between
132 dopaminergic pacemaker activity and uptake, we simulated DA dynamics in the DS
133 generated by pacemaker activity (4 Hz) of 150 neurons in the midbrain in a 100x100x100 µm
134 space (Fig. 1d, see parameters in Table 1). Our simulations yielded a pattern of partially
135 segregated DA hot spots with large fractions of the simulated space devoid of DA, suggesting
136 that release events in DS only elevate DA in the immediate surroundings with DAT-
137 dependent clearance preventing a larger spread in space (Fig. 1d). This was also illustrated by
138 a cross-section in time (Fig. 1e). In line with our recent in vivo microdialysis experiments, the
139 average DA concentration in the simulations during pacemaker activity was approximately
140 10 nM[40]. Further, when we calculated the average concentration of a larger area across time,

141 which fibre photometry conceivably does, the results resembled a tonic DA concentration
142 (Extended Data Fig. 1a). However, our model predicted a spatial distribution that is highly
143 heterogenous and devoid of pervasive resting or tonic DA levels (Fig. 1d-f).
144 To ensure our simulations were performed within a sufficiently large space to yield
145 consistent results, we tested different sizes of the simulated area and found a diameter of 50
146 μm to faithfully mimic the results of larger simulations (Extended Data Fig. 2a, b).
147 Additionally, we tested our simulations at different granularity (0.1, 0.5, 1 and 2 μm). The
148 finer the spatial grain, the higher detail close to a release event; however, at a spatial
149 granularity of 1 μm, [DA] deviated by <2% across most percentiles and only by >1 nM above
150 the 99.5th percentile (Extended Data Fig. 2c-f), leading us to use this voxel size for our
151 simulations.
152

153 ## Burst firing and receptor occupancy

154 DA cell bodies are known to fire short bursts of APs, which is a phenomenon strongly linked
155 to reward-prediction error and learning[8]. To gain insights into accompanying extracellular
156 DA dynamics, we simulated three different firing scenarios for a group of terminals within a
157 10x10x10 μm field encompassing roughly 40 release sites from the randomly simulated 150
158 neurons: 3 pulses at 10 Hz, 6 pulses at 20 Hz and 12 pulses at 40 Hz (Fig. 1g – burst
159 properties matched to be the same duration). Unsurprisingly, peak DA concentration was
160 reached at the end of the bursts (Fig. 1g). The 3 APs/10 Hz bursting scenario generated no
161 significant spill-over of DA outside the region of activity, whereas the 6 APs/20 Hz and 12
162 APs/40 Hz bursting scenarios markedly overwhelmed uptake (Fig. 1g). The relationship
163 between firing rate and the sphere of influence by DA became further evident when plotting
164 maximal concentration of the surrounding space (Fig. 1h) and the volume of space with a DA
165 concentration above 100 nM (Extended Data Fig. 1d). We found that the 3 APs/10 Hz

166 stimulation produced DA responses that largely resembled that of a single pulse. In both
167 cases, DA was mostly cleared after 100 ms and the volume exposed to greater than 100 nM
168 was similar (Fig. 1g and Extended Data Fig. 1d). In contrast, the high bursting activities
169 caused a frequency-dependent spill-over, where the areas exposed to a DA concentration
170 above 100 nM were 10 and 30 times larger than the terminal origin for 6 APs/20 Hz and 12
171 APs/40 Hz, respectively. Even after 100 ms, a considerable amount of DA remained in the 12
172 APs/40 Hz scenario (Fig. 1g).

173 To understand how these DA dynamics could affect the postsynaptic response, we
174 modelled receptor binding. D1 receptors (-Rs) were assumed to have a half maximal effective
175 concentration (EC_{50}) of 1000 nM and we extrapolated the reverse rate constant (K_{off}) to 19.5
176 s^{-1} based on a linear fit of the recently characterized DA receptor-based sensors (Extended
177 Data Fig. 1e) [41]. We set the EC_{50} of D2Rs to 7 nM and K_{off} to 0.2 s^{-1} based on the DA sensor
178 kinetic fit (Extended Data Fig. 1e), which matches a recent binding study[42]. To determine
179 how these receptors would respond to our predicted DA dynamics, we simulated pacemaker
180 activity at 4 Hz with an added burst of 6 APs/20 Hz. Fig. 1i shows a representative trace of
181 DA concentration and occupancy of the D1R and D2R within 1 μm of a release site. During
182 pacemaker activity, D1R showed an occupancy close to 0, whereas D2R occupancy was
183 approximately 0.65 (Fig. 1i). Both D1Rs and D2Rs occupancies were largely invariant to
184 individual release events caused by pacemaker activity. However, upon coordinated burst
185 firing, the occupancy rapidly increased (Fig. 1i). D1R receptor occupancy closely tracked
186 extracellular DA with a delay of only ~50 ms (Extended Data Fig. 1f). In contrast, it took at
187 least 5 seconds before the burst-induced increase in D2R occupancy had declined to baseline
188 levels (Fig. 1i), and, perhaps more surprisingly, the D2R occupancy only fell from 0.55 to
189 0.45 when simulating a full second pause in firing due to the slow off kinetics (Fig. 1j).

190 These simulations suggest that the dopaminergic architecture of the DS limits DA
191 overflow during physiologically relevant bursting activity. Further, DA receptors had a
192 temporally mostly uniform response to DA release caused by pacemaker activity with D1R
193 occupancy responding rapidly to both onset and offset extracellular DA concentrations
194 following bursts, while D2R showed seconds-long delays in offset.
195

196 ## Ventral striatum maintains pervasive DA tone

197 Mounting evidence points to considerable differences in DA dynamics across striatal
198 subregions[12,43], which might reflect differences in the cytoarchitectural and/or molecular
199 dopaminergic make up. In line with this, most studies report lower dopaminergic density in
200 the VS than in DS regardless of methodological modality with a median value of ~90% in VS
201 relative to DS (Extended Data Table 1). Further, DAT-mediated uptake capacity is reported
202 to be lower in VS with a median capacity at ~30% of DS (Extended Data Table 2).
203 Consistently, we observed a clear dorsoventral gradient for DAT expression when analysing
204 immunostainings in striatal mouse brain slices from a previous publication (Sørensen et al.,
205 2021[44]) (Extended Data Fig. 3a, b). By contrast, the VMAT2 staining only decreased slightly
206 from VS to DS (Extended Data Fig. 3a-c).
207 We simulated DA release during pacemaker activity in both DS and VS. DS values
208 were set as previously described (25 μm^3 per terminal, uptake capacity of 6.0 $\mu M\ s^{-1}$), but for
209 VS we reduced the terminal density to 90% (27.8 μm^3 per terminal) and DAT uptake
210 capacity to 33% (2.0 $\mu M\ s^{-1}$) (Extended Tables 1 and 2). The remaining parameters were kept
211 identical. With these two differences, our simulations revealed markedly different
212 spatiotemporal DA distributions during pacemaker activity. While DS formed segregated
213 domains with low DA concentrations in the inter-domain space (Fig. 2a), DA diffused further

214 throughout the simulated space in VS, before being cleared by DAT. This gave rise to what
215 may be considered a tonic DA level with hotspots of higher DA concentrations (Fig. 2a, b).
216 We compared our model of the two regions with existing experimental data. In an
217 earlier study by May and Wightman, 120 stimulus pulses were delivered in the medial
218 forebrain bundle (MFB) at either 10, 30 or 60 Hz and DA responses were recorded by FSCV
219 in both caudate-putamen (CPu) and nucleus accumbens (NAc)[45]. To mirror this, we simulated
220 120 action potentials at similar frequencies (10, 30, and 60 Hz) at 6% release probability and
221 ran the result through convolution, as in Extended Data Fig. 1b and c, to generate an FSCV
222 read-out (Fig. 2e). Since May and Wightman reported no significant difference in DA
223 released per electrically delivered pulse ($[DA]_p$) between VS and DS, we applied equal
224 quantal size and $R_{\%}$ for DS and VS in our simulations, while uptake capacity in VS was kept
225 to a third of DS and terminal density was set to 90% as specified above. Importantly, our
226 simulated FSCV data closely resembled the earlier findings, with VS reaching considerably
227 higher DA levels for all three stimulation frequencies (Fig. 2e). This regional difference
228 presumably arises from differences in DAT capacity between DS and VS, as the lower
229 terminal density in VS would have the opposite effect (see below) and the remaining
230 parameters were held identical.
231 To compare with our results for DS, we tested how VS responded during simulated
232 burst activity. Using firing patterns identical to the DS simulations (Fig. 1g), we found a
233 larger spill-over of DA into the surrounding areas in VS (Fig. 2f and Extended data Fig. 3d,
234 e). Significant amounts of extracellular DA also remained 100 ms after the physiologically
235 relevant 6APs/20Hz firing stimulus. At the receptor level, D1R occupancy in VS showed a
236 similar response to that in DS during the burst (Fig. 1i and 2g). By contrast, D2R occupancy
237 during pacemaker activity was higher in VS than DS (~0.8 versus ~0.65 in DS), in
238 accordance with the higher prevailing basal DA concentration. Additionally, the larger DA

239 overflow in VS after a burst caused a higher relative increase in receptor occupancy further
240 away from the area actively bursting than compared to DS (Fig. 2h). A pause in firing had the
241 same effect on D2R as in DS (Extended Data Fig. 3f).
242

243 ## Testing sensitivity of model parameters

244 To test the robustness of the results, we performed simulations across wide ranges of the
245 variable key parameters on which the model is based. First, we varied the number of
246 varicosities actively releasing DA by setting the varicosity density to one site per 9 μm^3 [28]
247 and simulating 4 Hz pacemaker activity with the release fraction ranging from 5% to 100%
248 (reported values range from 20% to virtually all)[10,46–48] (Fig. 3a). As the fraction of active
249 sites increased, DA concentrations increased at both the median level (50th percentile), which
250 we consider a measure of tonic or baseline DA levels, and at peak levels (99.5^{th} percentile) in
251 both DS and VS (Fig. 3b, see Extended Data Fig. 4a for schematic of tonic and peak DA).
252 We then used the $99.5^{th}/50^{th}$ percentile ratio as a measure of the focality of the DA
253 distribution (i.e. hotspot DA relative to baseline DA). Quantifying this across the percentage
254 of active terminals showed that the focality of the DA distribution dropped as the active
255 fraction increased in both regions (Fig. 3c). However, the percentage of active sites in VS
256 needed to drop to 5% to reach a relative distribution resembling the DS at a full 100% active
257 sites, underscoring a marked difference in the spatial confinement of DA signals in VS and
258 DS.

259 The predicted total DA content of a vesicle and the fraction of content released per
260 fusion event is reported to range from 1,000 to 30,000 molecules[49–52] (Fig. 3d). As expected,
261 tonic and peak concentrations increased in both DS and VS as quantal size was increased
262 (Fig. 3e). Also as expected, the focality of the DA distributions dropped for both regions as
263 quantal size increased (Fig. 3f). The relative difference in tonic DA, however, remained

264 persistently higher in VS and even increased as quantal size increased, indicating a tendency
265 for VS to maintain basal levels of DA regardless of release content (Fig. 3g). The higher end
266 of quantal sizes, however, resulted in median concentrations far beyond what is typically
267 reported (Fig. 3e)[5]. We observed largely similar pattern when changing either release
268 probability or firing rate (Extended Data Fig. 4b-g).

269 DAT activity is governed by two parameters: K_m and V_{max}[53]. To mimic competitive
270 inhibition of DAT by e.g., cocaine, we ran a simulation across various K_m values (Fig. 3h)
271 showing that increasing K_m caused a linear increase in DA levels, consistent with DAT
272 uptake rate responding almost linearly to increases in [DA] below K_m (Fig. 3i). Of note, most
273 microdialysis studies have reported that cocaine increases [DA] to the same degree in both
274 DS and VS; however, these quantifications are usually derived as a ratio of the absolute
275 baseline level[54,55]. If we divide our simulations of increasing K_m with the basal levels
276 estimated in Fig. 3a-c a similar response for DS and VS is found (Extended Data Fig. 5a).
277 Further, we observe a convergence on a two-fold difference in the absolute values at both
278 tonic and peak levels, which matches reports from earlier FSCV studies (Extended Data Fig.
279 5b)[56]. This regionally differential response to cocaine matches our observations in a previous
280 biosensor-based study[12].

281 Finally, we changed V_{max} by ± 50% in both regions and observed a smaller change in
282 for tonic level in DS (11 nM) than in VS (38 nM) (Fig. 3k). This suggests modulation of V_{max}
283 has higher impact in VS than DS. Further, the cusp-like behaviour of V_{max} in VS was
284 independent of both Q and $R_{\%}$ within values typically reported in the literature (Extended
285 Data Fig. 5c, d). In contrast to the changes in tonic levels, the relative effect V_{max} had on peak
286 levels was much more modest (Fig. 3l).

287 Changes to uptake rate may be mediated by DAT internalization pathways but to our
288 knowledge there is no in vivo evidence of differential release-uptake balances between

289 animals that could lead to varying tonic DA levels across animals. We therefore reanalysed
290 data from our previously published comparison of fibre photometry and microdialysis and
291 found evidence of natural variations in the release-uptake balance of the mice (Extended Data
292 Fig. 5f, g), which may underlie different tonic levels of DA in the striatum between animals.
293

294 ## Simulations of DAT nanoclustering

295 Our simulations highlight DAT V_{max} as an effective regulator of extracellular DA levels in
296 VS (Fig. 3k). Internalization of DAT can serve as a mechanism for this control but is a
297 relatively slow process operating on the order of minutes[53]. Interestingly, our recent studies
298 have provided evidence that DAT move laterally in the plasma membrane and transition from
299 a clustered to an unclustered nanoscale distribution in response to excitatory drive and other
300 inputs[57,58]. This led us to hypothesize that DAT nanoclustering serve as a mechanism for
301 regulating DAT activity on a faster time scale. We speculated that dense nanoclusters of DAT
302 would produce domains of low [DA] due to uptake overpowering diffusion (Fig. 4a). As
303 uptake rate is concentration dependent, this would reduce uptake efficiency (Fig. 4b). To
304 address this hypothesis, we simulated a single ellipsoid varicosity of 1.5 µm in length and
305 800 nm thick with surrounding extracellular space[48]. The surface was unfolded to a square of
306 equal area (Fig. 4c), and as 9-16.4% of terminals in the striatum are estimated to be
307 dopaminergic (Hökfelt, 1968; Tennyson et al., 1974), we set the volume of the surrounding
308 space to seven times the varicosity volume. On the surface of the varicosity, we randomly
309 distributed eight DAT nanoclusters (Fig. 4c) and ran simulations of how DAT clustering
310 density influenced the DA clearance from the surrounding space. The observed DA
311 concentration in the space surrounding the varicosity shown in Fig. 4c is illustrated by the
312 cross-section shown in Fig. 4d. Mean DA uptake capacity of the entire space was kept
313 constant at 4 µM s^{-1} (between the values observed for DS and VS) throughout the

314 simulations, representing a constant amount of DAT molecules on the surface of the
315 varicosity. We only changed the fraction of the surface of the varicosity that was uptake
316 competent by altering the cluster size from small clusters of high density to large clusters of
317 lower density. We ran simulations of eight clusters at 20, 40, 80 or 160 nm in diameter to
318 mirror experimentally observed cluster sizes on DA varicosities, as well as a scenario with
319 DAT fully dispersed (Fig. 4e)[57,58]. We then set the extracellular space to a [DA] of 100 nM
320 and simulated uptake for the four cluster sizes and an unclustered distribution of DAT. As
321 shown in Fig. 4f, the distribution of DAT into clusters of increasing density resulted in
322 progressively slower DA clearance. Thus, the unclustered scenario reduced [DA] to 10 nM in
323 just above 200 ms, whereas the 20 nm clusters took ~400 ms. As cluster size increased and
324 DAT density decreased, clearance time approached that of the fully unclustered scenario (Fig.
325 4g). The resulting hyper-local low-[DA] environment that came from dense DAT clusters
326 was apparent when we plotted the [DA] at the centre of a cluster compared to the mean [DA]
327 of the extracellular space (Fig. 4h). For the 20 nm cluster-scenario, the clearance was almost
328 entirely limited by how quickly DA diffused to the nanocluster, as the local [DA] dropped to
329 near zero. We originally hypothesized the effect would mainly be due to a depression in [DA]
330 at the cluster centre, but a concentration profile of the 80 nm cluster-scenario revealed the
331 entirety of the cluster was enveloped in a low-[DA] environment (Fig. 4i).
332 Summarized, the data supports that dense DAT nanoclusters produce domains of low
333 [DA] as uptake outcompetes diffusion. With transporter uptake being concentration
334 dependent, uptake efficiency is reduced. The simulations therefore posit DAT nanoclustering
335 as an efficient way to regulate the extracellular levels of tonic DA, particularly in VS.
336

337 ## DAT clusters more in the ventral striatum

338 As our simulations suggest that nanodomain clustering is a way of regulating uptake, and this
339 may be particularly efficient at controlling extracellular DA in VS, we hypothesized
340 nanoscale clustering would be more prominent in VS. To investigate this, we reanalysed data
341 from a previous publication[44], where we acquired super-resolution images of coronally sliced
342 striatal sections from mice stained for DAT. For the present study, images were split in DS
343 and VS based on where in the slices they were taken (Fig. 4j). DA terminals were identified
344 by vesicular monoamine transporter 2 (VMAT2) expression, and qualitatively DAT appeared
345 more clustered in VS than DS (Fig. 4k). To quantify this, we applied the clustering algorithm
346 Density-Based Spatial Clustering of Applications with Noise (DBSCAN) (Fig. 4l). This
347 confirmed a regional difference with more DAT localized to mean cluster size of 80 nm in
348 VS compared to DS (Fig. 4m), and we observed a similar regional difference across the range
349 of sizes typically reported (Fig. 4n)[57,58], supporting the conclusion that DAT nanoclustering is
350 more prevalent in VS than DS.

351 ## Discussion

352 We developed a three-dimensional, finite-difference computational model to investigate
353 spatiotemporal DA dynamics of striatal subregions in detail. Leveraging prior experimental
354 information on regional differences in dopaminergic innervation density and DAT uptake
355 capacity, our model predicts important differences in dopaminergic dynamics between DS
356 and VS. Strikingly, our simulations suggest that large areas of the DS are effectively devoid
357 of a basal level of DA at pacemaker activity, whereas VS maintain a more homogenous tonic-
358 like basal DA concentration with only small changes in uptake activity powerfully regulating
359 the extracellular DA tone. Furthermore, we modelled receptor binding kinetics and found that
360 D1R binding faithfully followed recently described rapid DA dynamics of the striatum[12,13,61],
361 while D2R, with an off-rate of ~5 seconds, appeared better suited for detecting background
362 tone, ramps and integrating prolonged activity[12,62]. Collectively, these observations have
363 important implications for our understanding of striatal function in behaviour, including
364 decoding of inputs from the prefrontal cortex (PFC) and limbic system as well as the
365 influential phasic-tonic model of dopaminergic signalling[8,9,63].

366 It has been assumed for long that there are tonic levels of DA in the striatum[5,8,9],
367 although the phenomenon has no clear definition[1]. Our simulation of DA dynamics in DS
368 during pacemaker-activity showed no evidence for a homogenous extracellular distribution.
369 Rather, elevated [DA] was transiently present around release sites during pacemaker activity
370 with the remaining space mostly depleted of DA. The absence of a general tonic DA level in
371 DS predicted by our model directly supports the notion that DA release sites in DS establish
372 distinct and only partially overlapping DA domains rather than diffuse, tonic DA levels (see
373 Liu et al., 2021[10]). This conclusion aligns with recent data where we found that DA
374 concentrations measured by microdialysis correlates with the average of rapid activity
375 recorded with fibre photometry rather than a baseline DA tone[13].

376 In contrast to the DS, our model predicted VS to hold a considerable basal level of
377 DA even in spaces without an immediately adjacent release site. This is conceivably what
378 most refer to as tonic DA. In this study, we quantified tonic DA as the median concentration
379 of the entire space (50th percentile), which appeared significantly higher in VS than DS
380 because of the lower VS uptake capacity. Importantly, this matches the results of our direct in
381 vivo comparison of DS and VS in freely moving mice[12]. To challenge our model, we
382 performed our simulations across a wide range of parameters. Only changes to V_{max} for
383 uptake generated differential responses in the two regions. With release and uptake
384 parameters at values from the literature, VS was at a critical point where minor changes to
385 uptake significantly impacted the tonic levels without any major effect on peak
386 concentrations.

387 Contrary to our observations, some previous microdialysis experiments have
388 suggested higher basal DA levels in the DS compared to VS (Kuczenski & Segal, 1992; Shen
389 et al., 2004 have reported 2-4 times higher [DA] in DS compared to VS[64,65]). However, there
390 are disparate observations in the literature (e.g. Carboni et al., 2001 reported 20% higher
391 [DA] in VS[54]). Moreover, it is important to note that regional comparisons in microdialysis
392 might be confounded by the considerably higher uptake rate in DS. This will increase the
393 extraction fraction and possibly lead to a significant overestimation of the extracellular
394 concentration as compared to a region with lower uptake rate, such as the VS[66].

395 Our three-dimensional simulations highlight DAT-mediated reuptake as a key
396 mechanism governing striatal DA dynamics and as a key mediator of regional-specific DA
397 dynamics. A physiologically relevant way to regulate uptake capacity is moving DAT to-and-
398 from the plasma membrane. Indeed, DAT is subject to such regulation and some of these
399 mechanisms may even be exclusive to the ventral region, including protein kinase C-induced
400 DAT internalization and Vav2 regulation of DAT surface expression[67,68]. Chemogenetic G_q-

401 coupled DREADD activation of DA neurons also result in differential DAT trafficking in the
402 two regions[69]. The findings position DAT regulation as an excellent candidate for changing
403 tonic DA levels in VS, which has been proposed to selectively attenuate afferent drive from
404 the PFC through D2R activation[63]. Recent studies of D2R expressing spiny projection
405 neurons (SPNs) in the VS also suggest that the receptor is not fully saturated under basal
406 firing[70], matching both our simulations of receptor binding and the notion that tonic DA can
407 be manipulated to alter D2R activation.

408 If changing uptake capacity is to have a behavioural relevance on a fast timescale, a
409 mechanism to regulate DAT function faster than internalization must exist. Importantly, the
410 transporter does not only move to-and-from the surface, but also laterally in the plasma
411 membrane. We have reported that DAT forms nanoclusters in the plasma membrane that
412 dynamically reshape based on excitatory and inhibitory input[57,58]. Moreover, we have
413 previously shown that cocaine, which both competitively inhibits DAT and reorganizes the
414 transporter nanodomains[58], changes the DA signal of the DS to dynamics akin to the VS[12].
415 Importantly, our simulations showed that nanoclustering may be an effective way to
416 sequester DAT in a dense domain where uptake overpowers diffusion and as a result brings
417 down effective uptake speed through microdomain DA depletion. We also found that the
418 nanoclustering phenomenon was considerably more prevalent in VS than in DS. Taken
419 together, these data point to DAT nanoclustering as a way to shape tonic levels of DA in the
420 striatum – particularly in the VS.

421 Our incorporation of receptor binding was inspired by previous data[22,23,71]. Dreyer &
422 colleagues assumed instantaneous equilibrium between extracellular DA and receptor
423 occupation while Hunger & colleagues based their kinetics on early pharmacological
424 studies[72–75]. However, we based our receptor kinetics on newer pharmacological experiments
425 in live cells[42] and properties of the recently developed DA receptor-based biosensors[41].

426 Indeed, these sensors are mutated receptors but only on the intracellular domains with no
427 changes of the binding site [41]. Overall, they exhibit kinetics that are well aligned with both
428 modelled and experimentally reported extracellular DA dynamics using non-biosensor-based
429 methods[3,37,76].

430 The presented simulations suggested that receptor binding was largely invariant to
431 single release events during pacemaker activity, while bursts of activity rapidly changed
432 occupancy. Both D1R and D2R immediately responded to burst onset; however, while D1R
433 occupancy rapidly declined to zero within approximately 50 ms, the slow D2R kinetics
434 resulted in an occupancy decline over ~5 seconds, returning to the baseline maintained by
435 tonic firing. This means that D1R is better suited to discriminate inputs in rapid succession
436 and allow for postsynaptic decoding of the fast-paced in vivo dynamics described in
437 particularly for DS[12,13,43]. By contrast, our analysis shows that D2Rs integrate DA signals
438 over several seconds. As D1R occupancy is negligible during pacemaker activity and D2R
439 kinetics are too slow to pick up rapid changes in DA concentration, our simulations moreover
440 suggest pauses in firing of less than 1 second is not an effective way of signalling for the
441 striatal dopaminergic system.

442 In conclusion, we have developed a three-dimensional model for DA release
443 dynamics and receptor binding that integrates a wealth of experimentally determined
444 parameters and generates responses to electrical and pharmacological input that fits robustly
445 with literature observations. The model offers an important theoretical framework and a
446 predictive tool that can serve as the basis for future experimental endeavours and help guide
447 the interpretation of new as well as older empirical findings on DA signalling dynamics under
448 both physiological conditions and in disease.

449 # Methods

450 ## Three-dimensional finite difference model

451 DA release sites in the striatum were simulated at a density of one site per 25 μm^3 in DS and
452 one site per 27.8 μm^3 in VS (except for Fig. 4b and c). As a single medium spiny neuron in
453 the striatum is estimated to be influenced by axons from 95 to 194 dopaminergic neurons[77],
454 we simulated DA release sites as originating from 150 separate cell bodies. These were set to
455 fire independently from each other at 4 Hz generated by a Poisson distribution. We set the
456 release probability in response to an action potential at the individual terminal levels to 6%[23],
457 and if a release occurred the DA concentration of the voxel was elevated by the equivalent of
458 3000 DA molecules as per Equation 1. The volume of each voxel was corrected for an
459 extracellular volume fraction of 0.21[78].

460 We did not incorporate paired-pulse depression in our model as most in vivo FSCV
461 studies have not reported this phenomenon[45,79–81]. In addition, we could explain the gradual
462 blunt of the response during prolonged stimulation (Fig. 2e) as the result of an equilibrium
463 between release and uptake rather than a depression in release. Newer in vivo biosensor-
464 based studies observe the same "blunting" phenomenon during stimulation trains[82]. A low
465 initial release probability that scales well with frequency has also been reported for VMAT2-
466 positive release sites in dopaminergic cultures where the axons are not severed from their cell
467 bodies as in acute striatal slices[83]. Note that we did not explicitly model autoreceptor
468 inhibition at pacemaker activity. However, this value should be implicitly reflected in the in
469 vivo estimates we base our model on.

470 When simulating bursts or trains of stimulations, action potentials were added as
471 described for each simulation, but release probability was kept the same unless otherwise
472 noted. Uptake was evenly distributed throughout the simulation space with a V_{max} at 6 $\mu m\ s^{-1}$
473 for DS and 2 $\mu m\ s^{-1}$ for VS (see Extended Data Table S2) and a K_m at 210 nM[84] and

474 calculated for each voxel as per Equation 2. For each time step, *dt*, diffusion calculated with a
475 finite difference implementation of the Laplacian operator described in Equation 3 using a
476 diffusion coefficient corrected for tortuosity at 321.7 $\mu m^2 s^{-1}$. Periodic boundaries were used
477 to avoid edge issues with a simulation size of 50x50x50 µm unless otherwise noted. The
478 Python-based implementation of the model can be found as described in the Code and Data
479 Availability section.
480

481 ## Immunohistochemistry analysis

482 Analysed widefield images were obtained from (Sørensen et al., 2021[44]). The mouse striatum
483 slices were stained for either DAT or VMAT2 (see Sørensen et al., 2021 for slicing, fixation,
484 staining and imaging protocol[44]). Fluorescence intensities were extracted in a single
485 dorsoventral line parallel to the midline through the horizontally centre of the anterior
486 commissure using ImageJ v1.53q. for each slice. Data was vertically centred around the
487 anterior commissure. No background subtraction was performed.
488

489 ## FSCV modelling

490 FSCV recordings were modelled by convoluting a simulated DA response to a pseudo FSCV
491 trace. The impulse function used was as described in Venton et al. 2002[76]. In brief, the
492 impulse function was defined as $IF_{FSCV} = e^{-(t+1)(k_{-1}*t_s+k_{-2}*t_o)}$, where t is time, t_s is scan
493 time, t_o is oxidization time, and k_{-1} and k_{-2} desorption constants. t_s was set to 100 ms as
494 reported in May & Wightman, 1989[45] and t_o to 4 ms, which is half of the typically reported
495 symmetrical waveform length. The desorption constants (k_{-1} = 1.2 s^{-1} and k_{-2} = 12 s^{-1}) were
496 taken directly from Venton et al., 2002[76].

497

498 ## Nanocluster uptake modelling

499 Nanoclustering of DAT was simulated in Python. An ellipsoid-shaped varicosity of 1.5 µm in
500 length and 800 nm in width was modelled as a flat, square surface with a width of 1.8 µm to
501 match the total surface area[57,58]. As 9-16.4% of terminals in the striatum are estimated to be
502 dopaminergic[59,60], we set the height of the simulation space to 3.52 µm to generate an
503 extracellular volume seven times the size of the varicosity. Axons and cell bodies are likely a
504 non-negligible part of the striatal volume but omitted in this analysis due to a lack of
505 information in the literature (however, decreasing the share of striatal space taken up by DA
506 varicosities works in the direction of our hypothesis). Spatial granularity was set to 20 nm,
507 and we randomly placed eight non-overlapping locations for clusters on the simulated
508 varicosity. Uptake capacity per voxel for each clustering scenario was set so the mean uptake
509 of the entire space was 4 µm s^{-1}, which resulted in clusters with increased DAT density with
510 decreasing cluster size. We set the initial DA concentration of the entire space to 100 nM and
511 ran the simulation with a time step of $1.875e^{-7}$ s to avoid numerical instability. Diffusion
512 corrected for tortuosity was set to 321.7 μm^2 s^{-1} and calculated with a Laplacian operation as
513 described in Equation 3. Periodic boundaries were used to account for the varicosity being
514 circular and avoid issues at the edge of the simulation space. The full implementation in
515 Python can be found as described in the Code and Data Availability section.

516

517 ## Super-resolution clustering analysis

518 Super-resolved fluorescence microscopy dual color images from Sørensen et al., 2021[44] of
519 striatal brain slices from mice were analyzed based on their position in the dorsal or ventral
520 regions (Fig. 4j). Localizations were fitted using DAOSTORM[85] on the originally acquired

direct stochastic optical reconstruction microscopy (dSTORM) videos with the following settings: background sigma of 8, maximum likelihood estimation as the fitting error model, 20 peak identification iterations, an initial sigma estimate of 1.5 and a threshold adjusted to each imaging session. Each image was analysed for percentage of localizations within a cluster using density-based spatial clustering of applications with noise (DBSCAN)[86] using the Python package Scikit-learn 0.22[87]. To uncover broader trends, we scanned across a range of parameters: radius was run from 10 nm to 200 nm and number of localizations from 10 to 200. For Fig. 4m a diameter of 80 nm was chosen to match the size reported in Rahbek-Clemmensen et al. 2017[57].

Statistical Analysis

The statistical analyses performed can be found in the legends of each figure. Statistical analyses were performed using open-source python packages SciPy v1.5.2 and NumPy v1.18.1. Boxplots show the 25th and 75th percentile range and whiskers indicate up to 1.5 times the interquartile range. The remaining data points are plotted as individual outliers.

Code and data availability

Numerical implementation and code to run the simulations are available at: https://github.com/GetherLab/striatal-dopamine-modelling. All experimental data are from Ejdrup & Wellbourne-Wood et al., 2023[13] or Sørensen et al., 2021[44]. Corresponding authors on these papers should be consulted for data availability.

Acknowledgements

We thank Dr. Kenneth L. Madsen, University of Copenhagen for general input on our modelling and Dr. Nicolas Tritsch, New York University Grossman School of Medicine, for a fruitful discussion on the postsynaptic receptor properties and occupation. The work was supported by the Lundbeck Foundation grants R266-2017-4331 (UG), R276-2018-792 (UG), R359-2020-2301 (UG), R181-2014-3090 (FH) and R303-2018-3540 (FH).

Author contributions

ALE, FH and UG conceptualized the study. ALE built the model with help from JKD. ALE ran the simulations. MDL and SHJ provided technical input on experimental data. ALE drafted the manuscript. ALE, FH and UG wrote the final version of the manuscript with comments and suggestions from JKD, TWR and JWD. All authors critically evaluated the manuscript. FH and UG supervised the project.

Competing Interests

JKD is employed at H. Lundbeck A/S

References

1. Berke, J. D. What does dopamine mean? *Nature Neuroscience 2018 21:6* **21**, 787–793 (2018).
2. Klaus, A., Alves Da Silva, J. & Costa, R. M. What, If, and When to Move: Basal Ganglia Circuits and Self-Paced Action Initiation. *Annu Rev Neurosci* **42**, 459–483 (2019).
3. Gonon, F. *et al.* Geometry and kinetics of dopaminergic transmission in the rat striatum and in mice lacking the dopamine transporter. *Prog Brain Res* **125**, 291–302 (2000).
4. Cragg, S. J. & Rice, M. E. DAncing past the DAT at a DA synapse. *Trends Neurosci* **27**, 270–277 (2004).
5. Sulzer, D., Cragg, S. J. & Rice, M. E. Striatal dopamine neurotransmission: regulation of release and uptake. *Basal Ganglia* **6**, (2016).
6. Borroto-Escuela, D. O. *et al.* Brain Dopamine Transmission in Health and Parkinson's Disease: Modulation of Synaptic Transmission and Plasticity Through Volume Transmission and Dopamine Heteroreceptors. *Front Synaptic Neurosci* **10**, (2018).
7. Agnati, L. F., Bjelke, B. & Fuxe, K. Volume versus wiring transmission in the brain: a new theoretical frame for neuropsychopharmacology. *Med Res Rev* **15**, (1995).
8. Schultz, W. Multiple dopamine functions at different time courses. *Annu Rev Neurosci* **30**, (2007).
9. Niv, Y., Daw, N. D., Joel, D. & Dayan, P. Tonic dopamine: opportunity costs and the control of response vigor. *Psychopharmacology (Berl)* **191**, 507–520 (2007).
10. Liu, C., Goel, P. & Kaeser, P. S. Spatial and temporal scales of dopamine transmission. *Nat Rev Neurosci* (2021) doi:10.1038/s41583-021-00455-7.
11. Sippy, T. & Tritsch, N. X. Unraveling the dynamics of dopamine release and its actions on target cells. *Trends Neurosci* (2023) doi:10.1016/J.TINS.2022.12.005.
12. Jørgensen, S. H. *et al.* Behavioral encoding across timescales by region-specific dopamine dynamics. *Proceedings of the National Academy of Sciences* **120**, e2215230120 (2023).
13. Ejdrup, A. L. *et al.* Within-Mice Comparison of Microdialysis and Fiber Photometry-Recorded Dopamine Biosensor during Amphetamine Response. *ACS Chem Neurosci* **14**, (2023).
14. Cardozo, D. L. & Bean, B. P. Voltage-dependent calcium channels in rat midbrain dopamine neurons: modulation by dopamine and GABAB receptors. *J Neurophysiol* **74**, 1137–1148 (1995).
15. Threlfell, S. *et al.* Striatal muscarinic receptors promote activity dependence of dopamine transmission via distinct receptor subtypes on cholinergic interneurons in ventral versus dorsal striatum. *J Neurosci* **30**, 3398–3408 (2010).
16. Richards, T. L. & Zahniser, N. R. Rapid substrate-induced down-regulation in function and surface localization of dopamine transporters: rat dorsal striatum versus nucleus accumbens. *J Neurochem* **108**, 1575–1584 (2009).
17. Brown, H. D., McCutcheon, J. E., Cone, J. J., Ragozzino, M. E. & Roitman, M. F. Primary food reward and reward-predictive stimuli evoke different patterns of phasic dopamine signaling throughout the striatum. *Eur J Neurosci* **34**, (2011).
18. Kearney, P. J. *et al.* Presynaptic Gq-coupled receptors drive biphasic dopamine transporter trafficking that modulates dopamine clearance and motor function. *J Biol Chem* **299**, (2023).

19. Salinas, A. G. *et al.* Distinct sub-second dopamine signaling in dorsolateral striatum measured by a genetically-encoded fluorescent sensor. *Nature Communications 2023 14:1* **14**, 1–16 (2023).
20. Mohebi, A., Wei, W., Pelattini, L., Kim, K. & Berke, J. D. Dopamine transients follow a striatal gradient of reward time horizons. *Nature Neuroscience 2024* 1–10 (2024) doi:10.1038/s41593-023-01566-3.
21. Dodson, P. D. *et al.* Representation of spontaneous movement by dopaminergic neurons is cell-type selective and disrupted in parkinsonism. *Proc Natl Acad Sci U S A* **113**, E2180-8 (2016).
22. Dreyer, J. K. & Hounsgaard, J. Mathematical model of dopamine autoreceptors and uptake inhibitors and their influence on tonic and phasic dopamine signaling. *https://doi.org/10.1152/jn.00502.2012* (2013) doi:10.1152/jn.00502.2012.
23. Dreyer, J. K., Herrik, K. F., Berg, R. W. & Hounsgaard, J. D. Influence of phasic and tonic dopamine release on receptor activation. *Journal of Neuroscience* **30**, 14273–14283 (2010).
24. Beyene, A. G., McFarlane, I. R., Pinals, R. L. & Landry, M. P. Stochastic Simulation of Dopamine Neuromodulation for Implementation of Fluorescent Neurochemical Probes in the Striatal Extracellular Space. *ACS Chem Neurosci* **8**, 2275–2289 (2017).
25. Wiencke, K., Horstmann, A., Mathar, D., Villringer, A. & Neumann, J. Dopamine release, diffusion and uptake: A computational model for synaptic and volume transmission. *PLoS Comput Biol* **16**, e1008410 (2020).
26. Venton, B. J. *et al.* Real-time decoding of dopamine concentration changes in the caudate-putamen during tonic and phasic firing. *J Neurochem* **87**, 1284–1295 (2003).
27. Dreyer, J. K., M, V. W. C., Lovic, V. & Aragona, B. J. Functionally Distinct Dopamine Signals in Nucleus Accumbens Core and Shell in the Freely Moving Rat. *J Neurosci* **36**, (2016).
28. Doucet, G., Descarries, L. & Garcia, S. Quantification of the dopamine innervation in adult rat neostriatum. *Neuroscience* **19**, (1986).
29. Olson, L., Seiger, Å. & Fuxe, K. Heterogeneity of striatal and limbic dopamine innervation: Highly fluorescent islands in developing and adult rats. *Brain Res* **44**, 283–288 (1972).
30. Jones, S. R. *et al.* Profound neuronal plasticity in response to inactivation of the dopamine transporter. *Proc Natl Acad Sci U S A* **95**, 4029–4034 (1998).
31. Eriksen, J., Jørgensen, T. N. & Gether, U. Regulation of dopamine transporter function by protein-protein interactions: new discoveries and methodological challenges. *J Neurochem* **113**, 27–41 (2010).
32. Eriksen, J. *et al.* Visualization of dopamine transporter trafficking in live neurons by use of fluorescent cocaine analogs. *J Neurosci* **29**, 6794–6808 (2009).
33. Block, E. R. *et al.* Brain Region-Specific Trafficking of the Dopamine Transporter. *J Neurosci* **35**, 12845–12858 (2015).
34. Nicholson, C. Interaction between diffusion and Michaelis-Menten uptake of dopamine after iontophoresis in striatum. *Biophys J* **68**, 1699–1715 (1995).
35. Nicholson, C. Diffusion from an injected volume of a substance in brain tissue with arbitrary volume fraction and tortuosity. *Brain Res* **333**, 325–329 (1985).
36. Xie, K. *et al.* Organic electrochemical transistor arrays for real-time mapping of evoked neurotransmitter release in vivo. *Elife* **9**, (2020).
37. Atcherley, C. W. *et al.* Improved Calibration of Voltammetric Sensors for Studying Pharmacological Effects on Dopamine Transporter Kinetics in Vivo. *ACS Chem Neurosci* **6**, 1509–1516 (2014).

38. Brimblecombe, K. R. *et al.* Calbindin-D28K Limits Dopamine Release in Ventral but Not Dorsal Striatum by Regulating Ca2+ Availability and Dopamine Transporter Function. *ACS Chem Neurosci* **10**, 3419–3426 (2019).
39. Stuber, G. D., Hnasko, T. S., Britt, J. P., Edwards, R. H. & Bonci, A. Dopaminergic Terminals in the Nucleus Accumbens But Not the Dorsal Striatum Corelease Glutamate. *Journal of Neuroscience* **30**, 8229–8233 (2010).
40. Ejdrup, A. L. *et al.* Within-animal comparison of microdialysis and fiber photometry in amphetamine-exposed mice. *bioRxiv* 2022.10.27.513984 (2022) doi:10.1101/2022.10.27.513984.
41. Labouesse, M. A. & Patriarchi, T. A versatile GPCR toolkit to track in vivo neuromodulation: not a one-size-fits-all sensor. *Neuropsychopharmacology 2021 46:12* **46**, 2043–2047 (2021).
42. Ågren, R., Stepniewski, T. M., Zeberg, H., Selent, J. & Sahlholm, K. Dopamine d2 receptor agonist binding kinetics—role of a conserved serine residue. *Int J Mol Sci* **22**, (2021).
43. Wei, W., Mohebi, A. & Berke, J. D. A Spectrum of Time Horizons for Dopamine Signals. *bioRxiv* 2021.10.31.466705 (2022) doi:10.1101/2021.10.31.466705.
44. Sørensen, G. *et al.* Disruption of the PDZ domain-binding motif of the dopamine transporter uniquely alters nanoscale distribution, dopamine homeostasis, and reward motivation. *J Biol Chem* **297**, (2021).
45. May, L. J. & Wightman, R. M. Effects of D-2 antagonists on frequency-dependent stimulated dopamine overflow in nucleus accumbens and caudate-putamen. *J Neurochem* **53**, 898–906 (1989).
46. Pereira, D. B. *et al.* Fluorescent false neurotransmitter reveals functionally silent dopamine vesicle clusters in the striatum. *Nature Neuroscience 2016 19:4* **19**, 578–586 (2016).
47. Liu, C., Kershberg, L., Wang, J., Schneeberger, S. & Kaeser, P. S. Dopamine Secretion Is Mediated by Sparse Active Zone-like Release Sites. *Cell* **172**, 706-718.e15 (2018).
48. Ducrot, C. *et al.* Dopaminergic neurons establish a distinctive axonal arbor with a majority of non-synaptic terminals. *The FASEB Journal* **35**, e21791 (2021).
49. Garris, P. A., Ciolkowski, E. L., Pastore, P. & Wightman, F. M. Efflux of Dopamine from the Synaptic Cleft in the Nucleus Accumbens of the Rat Brain. (1994).
50. Staal, R. G. W., Mosharov, E. V. & Sulzer, D. Dopamine neurons release transmitter via a flickering fusion pore. *Nat Neurosci* **7**, 341–346 (2004).
51. Sulzer, D. & Pothos, E. N. Regulation of quantal size by presynaptic mechanisms. *Rev Neurosci* **11**, 159–212 (2000).
52. Pothos, E. N., Davila, V. & Sulzer, D. Presynaptic recording of quanta from midbrain dopamine neurons and modulation of the quantal size. *J Neurosci* **18**, 4106–4118 (1998).
53. Kristensen, A. S. *et al.* SLC6 neurotransmitter transporters: structure, function, and regulation. *Pharmacol Rev* **63**, 585–640 (2011).
54. Carboni, E. *et al.* Cocaine and Amphetamine Increase Extracellular Dopamine in the Nucleus Accumbens of Mice Lacking the Dopamine Transporter Gene. *Journal of Neuroscience* **21**, RC141–RC141 (2001).
55. Maisonneuve, I. M. & Glick, S. D. Interactions between ibogaine and cocaine in rats: in vivo microdialysis and motor behavior. *Eur J Pharmacol* **212**, 263–266 (1992).
56. Wu, Q., Reith, M. E. A., Kuhar, M. J., Carroll, F. I. & Garris, P. A. Preferential increases in nucleus accumbens dopamine after systemic cocaine administration are

704 caused by unique characteristics of dopamine neurotransmission. *J Neurosci* **21**, 6338–
705 6347 (2001).
706 57. Rahbek-Clemmensen, T. *et al.* Super-resolution microscopy reveals functional
707 organization of dopamine transporters into cholesterol and neuronal activity-dependent
708 nanodomains. *Nat Commun* **8**, 1–14 (2017).
709 58. Lycas, M. D. *et al.* Nanoscopic dopamine transporter distribution and conformation are
710 inversely regulated by excitatory drive and D2 autoreceptor activity. *Cell Rep* **40**,
711 111431 (2022).
712 59. Tennyson, V. M., Heikkila, R., Mytilineou, C., Côté, L. & Cohen, G. 5-
713 Hydroxydopamine 'tagged' neuronal boutons in rabbit neostriatum: interrelationship
714 between vesicles and axonal membrane. *Brain Res* **82**, 341–348 (1974).
715 60. Hökfelt, T. In vitro studies on central and peripheral monoamine neurons at the
716 ultrastructural level. *Z Zellforsch Mikrosk Anat* **91**, 1–74 (1968).
717 61. Markowitz, J. E. *et al.* Spontaneous behaviour is structured by reinforcement without
718 explicit reward. *Nature 2023 614:7946* **614**, 108–117 (2023).
719 62. Howe, M. W., Tierney, P. L., Sandberg, S. G., Phillips, P. E. M. & Graybiel, A. M.
720 Prolonged dopamine signalling in striatum signals proximity and value of distant
721 rewards. *Nature* **500**, 575–579 (2013).
722 63. Grace, A. A., Floresco, S. B., Goto, Y. & Lodge, D. J. Regulation of firing of
723 dopaminergic neurons and control of goal-directed behaviors. *Trends Neurosci* **30**,
724 220–227 (2007).
725 64. Kuczenski, R. & Segal, D. S. Differential effects of amphetamine and dopamine
726 uptake blockers (cocaine, nomifensine) on caudate and accumbens dialysate dopamine
727 and 3-methoxytyramine. *Journal of Pharmacology and Experimental Therapeutics*
728 **262**, (1992).
729 65. Shen, H. W. *et al.* Regional Differences in Extracellular Dopamine and Serotonin
730 Assessed by In Vivo Microdialysis in Mice Lacking Dopamine and/or Serotonin
731 Transporters. *Neuropsychopharmacology 2004 29:10* **29**, 1790–1799 (2004).
732 66. Chefer, V. I., Thompson, A. C., Zapata, A. & Shippenberg, T. S. Overview of Brain
733 Microdialysis. *Curr Protoc Neurosci* **47**, 7.1.1-7.1.28 (2009).
734 67. Fagan, R. R. *et al.* Dopamine transporter trafficking and Rit2 GTPase: Mechanism of
735 action and in vivo impact. *J Biol Chem* **295**, 5229–5244 (2020).
736 68. Zhu, S. *et al.* Identification of a Vav2-dependent mechanism for GDNF/Ret control of
737 mesolimbic DAT trafficking. *Nat Neurosci* **18**, 1084–1093 (2015).
738 69. Kearney, P. J. *et al.* Presynaptic Gq-coupled receptors drive biphasic dopamine
739 transporter trafficking that modulates dopamine clearance and motor function. *J Biol*
740 *Chem* **299**, 102900 (2023).
741 70. Lee, S. J. *et al.* Cell-type-specific asynchronous modulation of PKA by dopamine in
742 learning. *Nature 2020 590:7846* **590**, 451–456 (2020).
743 71. Hunger, L., Kumar, A. & Schmidt, R. Abundance Compensates Kinetics: Similar
744 Effect of Dopamine Signals on D1 and D2 Receptor Populations. *J Neurosci* **40**, 2868–
745 2881 (2020).
746 72. Nishikori, K., Noshiro, O., Sano, K. & Maeno, H. Characterization, Solubilization, and
747 Separation of T w o Distinct Dopamine Receptors in Canine Caudate Nucleus*.
748 *Journal of Biological Chemistry* **255**, 10909–10915 (1980).
749 73. Maeno, H. Dopamine receptors in canine caudate nucleus. *Mol Cell Biochem* **43**, 65–
750 80 (1982).
751 74. Sano, K., Noshiro, O., Katsuda, K., Nishikori, K. & Maeno, H. Dopamine receptors
752 and dopamine-sensitive adenylate cyclase in canine caudate nucleus. Characterization
753 and solubilization. *Biochem Pharmacol* **28**, 3617–3627 (1979).

75. Burt, D. R., Creese, I. & Snyder, S. H. Properties of [3H]Haloperidol and [3H]Dopamine Binding Associated with Dopamine Receptors in Calf Brain Membranes. *Mol Pharmacol* **12**, (1976).
76. Venton, B. J., Troyer, K. P. & Wightman, R. M. Response times of carbon fiber microelectrodes to dynamic changes in catecholamine concentration. *Anal Chem* **74**, 539–546 (2002).
77. Matsuda, W. *et al.* Single Nigrostriatal Dopaminergic Neurons Form Widely Spread and Highly Dense Axonal Arborizations in the Neostriatum. *Journal of Neuroscience* (2009) doi:10.1523/JNEUROSCI.4029-08.2009.
78. Rice, M. E. & Nicholson, C. Diffusion characteristics and extracellular volume fraction during normoxia and hypoxia in slices of rat neostriatum. *https://doi.org/10.1152/jn.1991.65.2.264* **65**, 264–272 (1991).
79. Garris, P. A. & Wightman, R. M. Different Kinetics Govern Dopaminergic Transmission in the Amygdala, Prefrontal Cortex, and Striatum: An in vivo Voltammetric Study. *The Journal of Neuroscience* **14**, 442–450 (1994).
80. Hamid, A. A. *et al.* Mesolimbic dopamine signals the value of work. *Nat Neurosci* **19**, 117–126 (2015).
81. Chergui, K., Suaud-Chagny, M. F. & Gonon, F. Nonlinear relationship between impulse flow, dopamine release and dopamine elimination in the rat brainin vivo. *Neuroscience* **62**, 641–645 (1994).
82. Mohebi, A., Collins, V. L. & Berke, J. D. Cholinergic Interneurons Drive Motivation by Promoting Dopamine Release in the Nucleus Accumbens. *bioRxiv* 2022.11.06.515335 (2022) doi:10.1101/2022.11.06.515335.
83. Silm, K. *et al.* Synaptic Vesicle Recycling Pathway Determines Neurotransmitter Content and Release Properties. *Neuron* **102**, 786-800.e5 (2019).
84. Hovde, M. J., Larson, G. H., Vaughan, R. A. & Foster, J. D. Model Systems for Analysis of Dopamine Transporter Function and Regulation. *Neurochem Int* **123**, 13 (2019).
85. Babcock, H., Sigal, Y. M. & Zhuang, X. A high-density 3D localization algorithm for stochastic optical reconstruction microscopy. *Opt Nanoscopy* **1**, 1–10 (2012).
86. Ester, M., Kriegel, H.-P., Sander, J. & Xu, X. A Density-Based Algorithm for Discovering Clusters in Large Spatial Databases with Noise. in *Proceedings of the 2nd International Conference on Knowledge Discovery and Data Mining* (1996).
87. Pedregosa, F. *et al.* Scikit-learn: Machine Learning in Python. *Journal of Machine Learning Research* **12**, 2825–2830 (2021).
88. Paladini, C. A., Robinson, S., Morikawa, H., Williams, J. T. & Palmiter, R. D. Dopamine controls the firing pattern of dopamine neurons via a network feedback mechanism. *Proc Natl Acad Sci U S A* **100**, 2866–2871 (2003).
89. Zhou, F. M., Liang, Y. & Dani, J. A. Endogenous nicotinic cholinergic activity regulates dopamine release in the striatum. *Nat Neurosci* **4**, 1224–1229 (2001).

Table 1 – List of variables used in simulation of the dorsal striatum.

Variable	Abbreviation	Value	Reference
Firing rate		4 Hz	[88]
Release probability		6%	[23]
DA molecules per vesicle		3000	[4]
Diffusion coefficient		763 $\mu m^2 s^{-1}$	[34]
Tortuosity		1.54	[78]
Vmax		6.0 $\mu m\ s^{-1}$	See Table S2
Km		210 nM	[84]
Active terminal density	-	0.04 μm^{-3}	[10]
Extracellular volume fraction		0.21	[78]
Number of neurons in simulation space	-	150	[77]

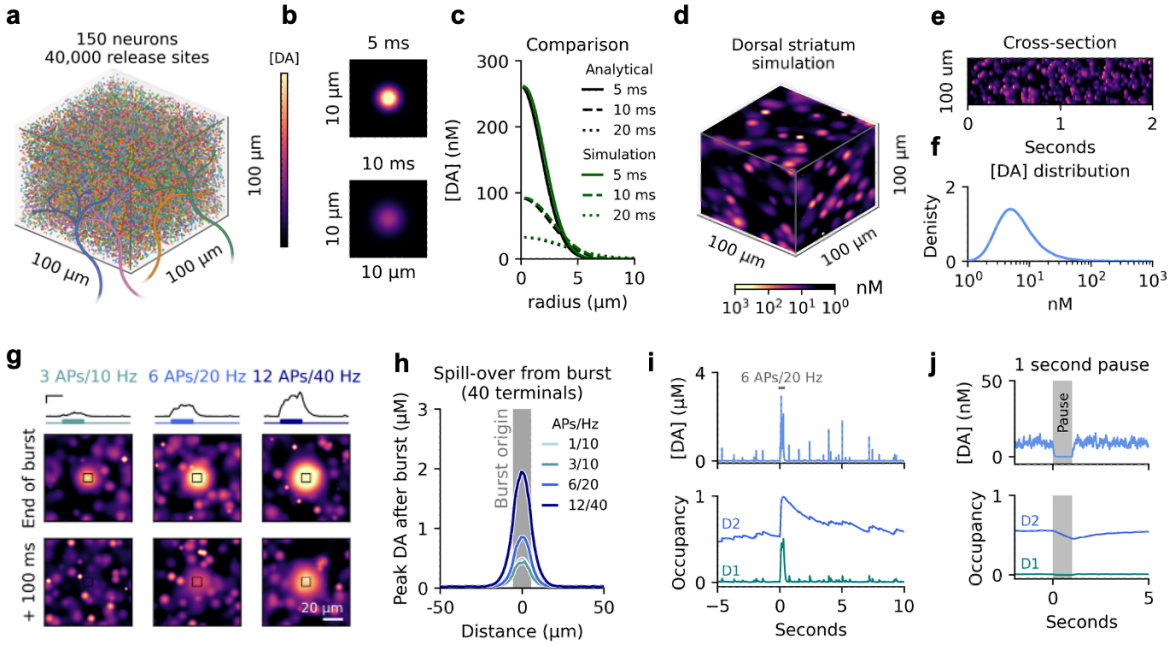

Fig. 1 – Large-scale 3D model of the dorsal striatum

a, Self-enveloped simulation space of 100^3 µm^3 with approximately 40.000 release sites from 150 neurons. Colours of individual release sites are not matched to neurons. **b,** Simulation of a single release event after 5 ms and 10 ms. Colour-coded by DA concentration. **c,** Comparison of analytical solution and simulation of diffusion after a single release event at three different time points. **d,** Representative snapshot of steady state DA dynamics at 4 Hz tonic firing with parameters mirroring the dorsal striatum. **e,** Cross-section of temporal dynamics for data shown in (d). **f,** Histogram of DA concentrations ([DA]) across the entire space in (d). **g,** DA release during three burst activity scenarios for all release sites in a 10x10x10 µm cube (black boxes) and spill-over into the surrounding space. Burst simulated as increase in firing rate on top of continued tonic firing of the surrounding space. Traces on top are average DA concentrations for the marked cubes, with bursts schematized by coloured lines below. First image row is at the end of the burst, second row another 100 ms after. Scale bars for traces are 200 ms and 500 nM. Scale bar for the images is 20 µm. **h,** Peak DA concentration reached at different distances from area with phasic activity for the three firing scenarios. **i,** Top: representative [DA] trace 1 µm away from a release site during pacemaker and burst activity. Bottom: Occupancy of D1Rs and D2Rs for same site. **j,** Effect of complete pause in firing for 1 second on both average [DA] and D1R and D2R occupation.

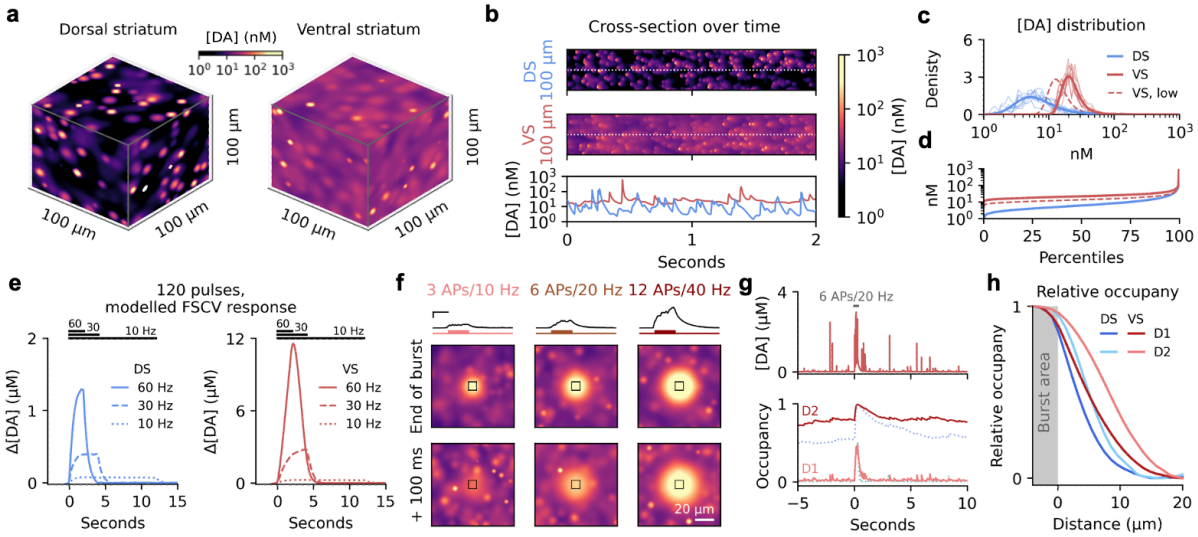

Fig. 2 – Regional difference in uptake greatly impact DA dynamics

a. Representative snapshots of steady state dynamics at 4 Hz tonic firing with parameters mirroring the dorsal (left) and ventral striatum (right). **b,** Cross-section of temporal dynamics for data shown in a. Bottom row show concentrations of the dashed lines in the top panels **c,** Normalized density of DA concentration of simulations in (a). Thick lines are for the entire space, thin lines are across time for five randomly sampled locations. Dashed red line is for simulation of the ventral striatum with lowest reported innervation density in the literature. **d,** Same data as in (c), but for concentration percentiles. Note that even the lowest percentiles of VS were above 10 nM in [DA]. **e,** Convoluted model response (extended data Fig. 1c) to mimic FSCV measurements mirroring the experimentally tested stimulation paradigm in [45] for the dorsal (left) and ventral striatum (right) **f,** DA release during three burst activity scenarios for all release sites in a 10x10x10 µm cube (black boxes) and spill-over into the surrounding space. Burst simulated as increase in firing rate on top of continued tonic firing of the surrounding space. Traces on top are average DA concentrations for the marked cubes, with bursts schematized by coloured lines below. First image row is at the end of the burst, second row another 100 ms after. Scale bars for traces are 200 ms and 500 nM. Scale bar for the images is 20 µm. **g,** Top: representative [DA] trace 1 µm away from a release site during pacemaker and burst activity. Bottom: Occupancy of D1Rs and D2Rs for same site. Occupancy data from corresponding DS simulation on Fig. 1k shown in as dotted line. **h,** Peak occupancy at different distances from the area bursting normalized to maximal and minimum occupancy.

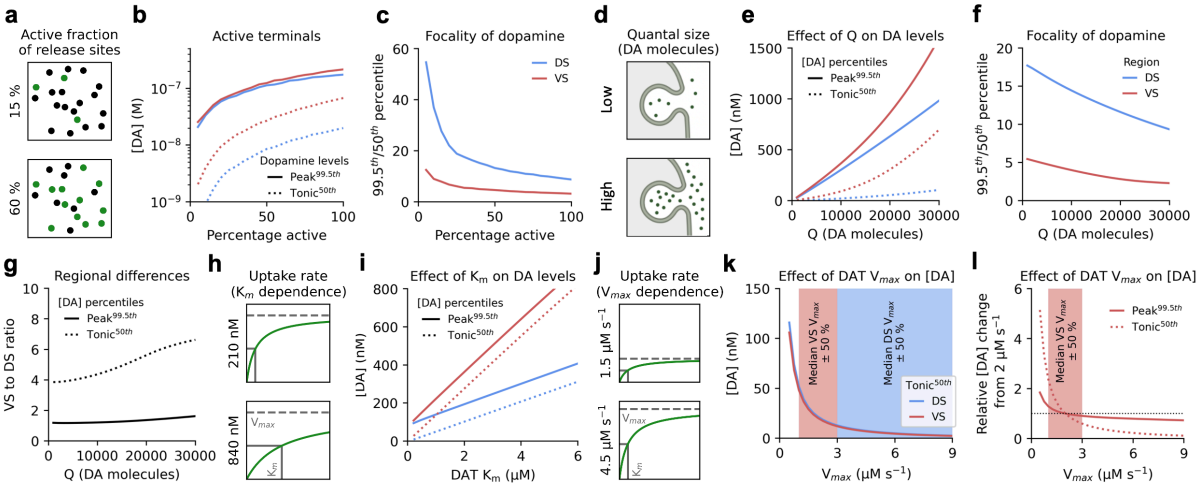

Fig. 3 – Sensitivity of the model to parameter changes

a, Schematic of the fraction of active release sites. Black dots are inactive sites and green dots indicate actively releasing sites. **b,** Effect of changing fraction of active release sites on DA concentrations. Blue line, DS peak DA concentration (99.5th percentile); Red line, VS peak DA concentration (99.5th percentile); Dotted blue line, DS tonic DA concentration (50th percentile); Dotted red line, VS tonic DA concentration (50th percentile).**c,** Ratio between peak (99.5th percentile) and tonic (50th percentile) concentrations across fractions of active release sites in the DS (blue line) and VS (red line) as a measure of DA signal focality. **d,** Schematic of changing quantal size (Q). **e,** Effect of changing quantal size on tonic and peak DA concentrations in DS (blue lines) and VS (red lines). **f,** Ratio between peak and tonic concentrations across various quantal sizes in in DS (blue line) and VS (red line). **g,** Relative difference between the DS and VS for peak (black line) and tonic DA (dotted line) at different quantal sizes. **h,** Schematic of changing DAT K_m. **i,** Effect of changing DAT K_m on DA concentrations in DS (blue lines) and VS (red lines). **j,** Schematic of changing DAT V_{max}. **k,** Effect of changing DAT V_{max} on DA concentrations. Shaded areas are median V_{max} of the two regions (DS and VS) as found in the literature shown in Table S2 ± 50%. **l,** Effect of changing DAT V_{max}, with tonic (50th percentile) and peak (99.5th percentile) DA concentrations normalized to their value at 2 μm s^{-1} (median value for VS). Shaded area indicates median V_{max} for VS found in the literature shown in Table S2 ± 50%.

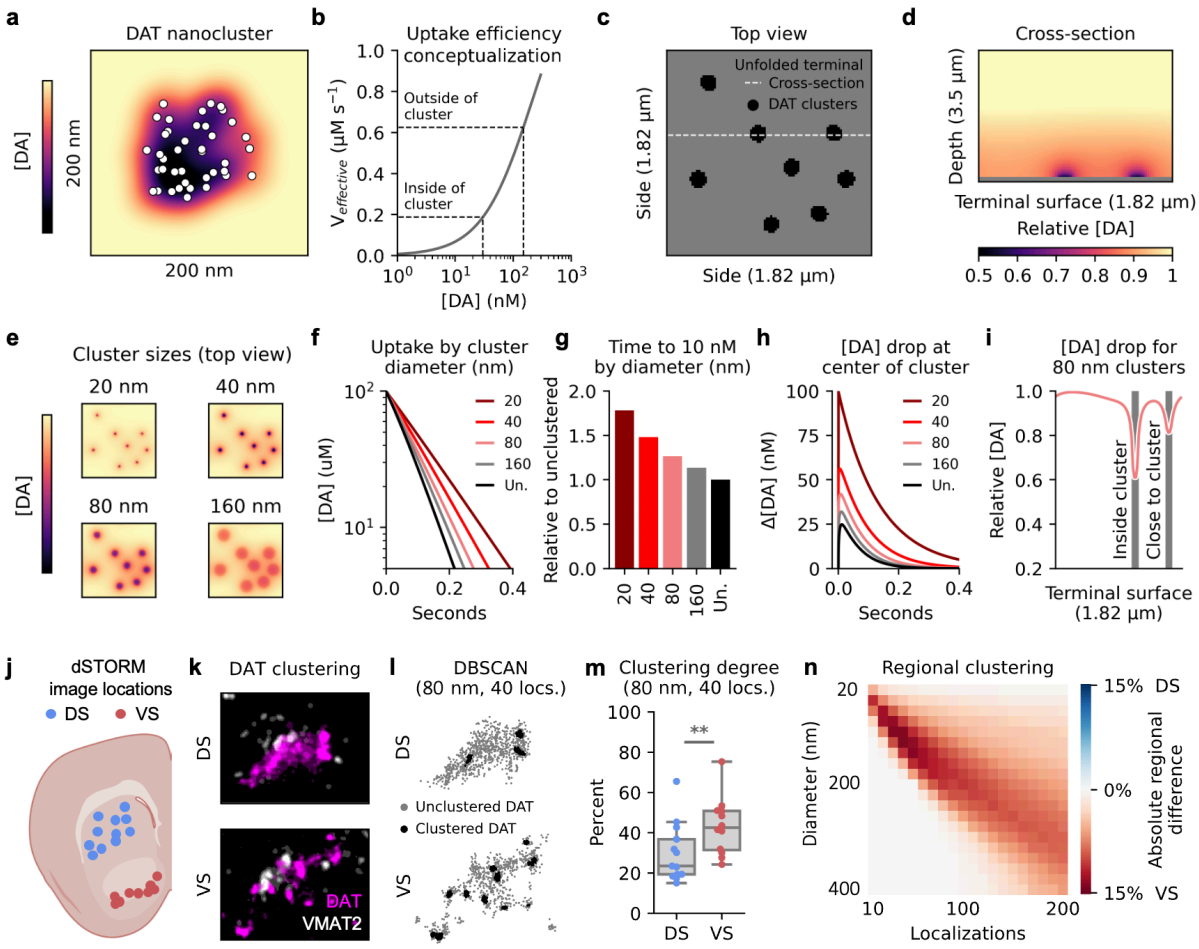

Fig. 4 – DAT nanoclustering reduces uptake and shows regional variation
a. Schematic of dense DA cluster. White dots represent individual DAT molecules, and colour gradient the surrounding DA concentration. **b,** Effective transport rate dependent on local concentration. **c,** Top view of unfolded DA varicosity. Black shapes denote clusters of DAT. Dashed white line indicates placement of cross-section shown in (d). **d,** Cross section showing DA concentration in space surrounding varicosity unfolded in c. Grey line at the bottom is surface of the varicosity. Colour-coded for DA concentration. **e,** Top view from (c), but colour coded for DA concentration immediately above membrane surface at different DAT cluster sizes. **f,** Mean [DA] over time for different DAT cluster sizes and unclustered (Un.). **g,** Time to reach a mean DA concentration of 10 nM for different DAT cluster sizes and unclustered (Un.). **h,** Difference between DA concentration at the centre of clusters and mean concentration throughout the simulation for different cluster sizes and unclustered (Un.). **i,** Concentrations across a cross section of a surface with 80 nm diameter clusters. Shaded areas highlight cluster locations. **j,** Location of images of the dorsal (DS) and ventral striatum (VS) in striatal slices from mice as imaged in (Sørensen et al., 2021[44]) with direct stochastic optical reconstruction microscopy (dSTORM). **k,** Two representative DA varicosities from DS and VS with VMAT2 in white and DAT in magenta. Images are 1.5x2 μm. **l,** Individual DAT localizations from images in (k) coloured by clustering. Black indicates localization identified as clustered based on DBSCAN with parameters 80 nm diameter and 40 localizations. Grey indicates unclustered localizations. **m,** Quantification of clustering across all images in (j) with parameters in (l). Welch's two-sample t-test, P = 0.012(*), n = 12 (DS) and 13 (VS). **n,** Absolute difference in percentage of clustering as assessed with DBSCAN across a range of parameters. VS has a higher propensity to cluster across cluster sizes typically reported for DAT clusters.

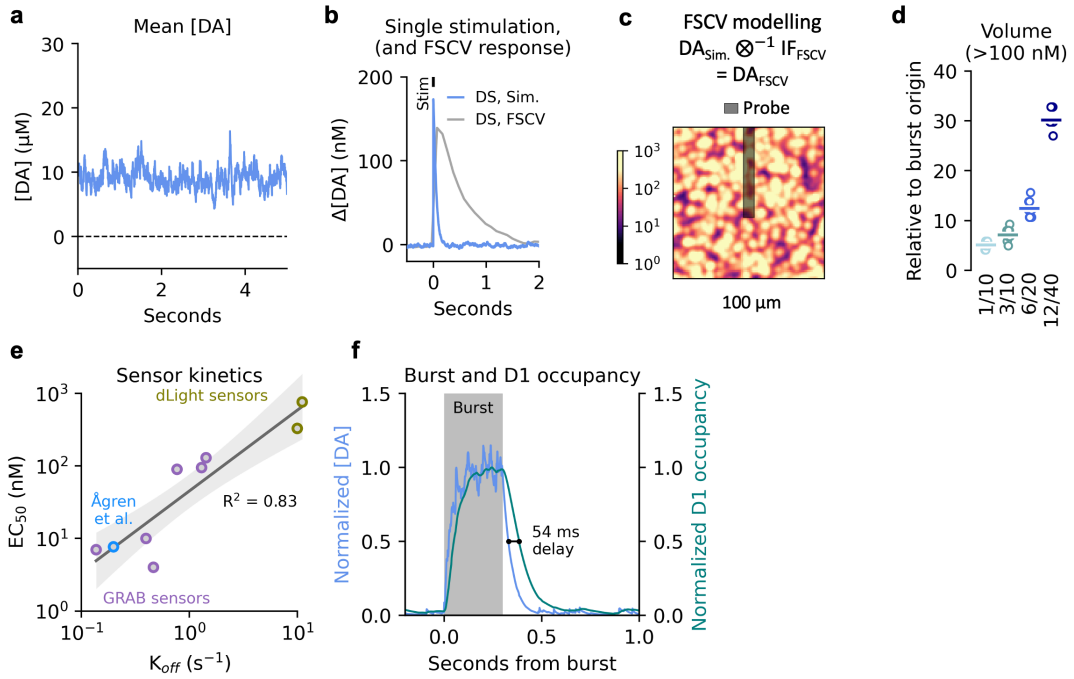

Extended Data Fig. 1 – Average concentration and receptor kinetics
a. Average DA concentration across a 100x100x100 μm volume of simulated DS at pacemaker activity. **b,** Mean concentration change in response to single event with 60% release probability (see supplementary notes on electrical stimulation) in all neurons at time zero. Blue trace is output directly from simulation, grey trace is the predicted FSCV measurement. **c,** Modelling of predicted FSCV measurement and representative snapshot of simulation space just after a release event. **d,** Volume of space exposed to greater than 100 nM DA after firing relative to volume of space where terminals actively burst. **e,** Least-square fit linear regression of the dLight and $GRAB_{DA}$ sensors based on reported kinetics[41] and newest experimental characterization of D2R[42]. Shaded are indicates 95% C.I. **f,** Zoom on a DA burst as on Fig. 1i, with [DA] in blue and D1R occupancy in teal. Shaded area indicates period of bursting with 6 APs at 20 Hz.

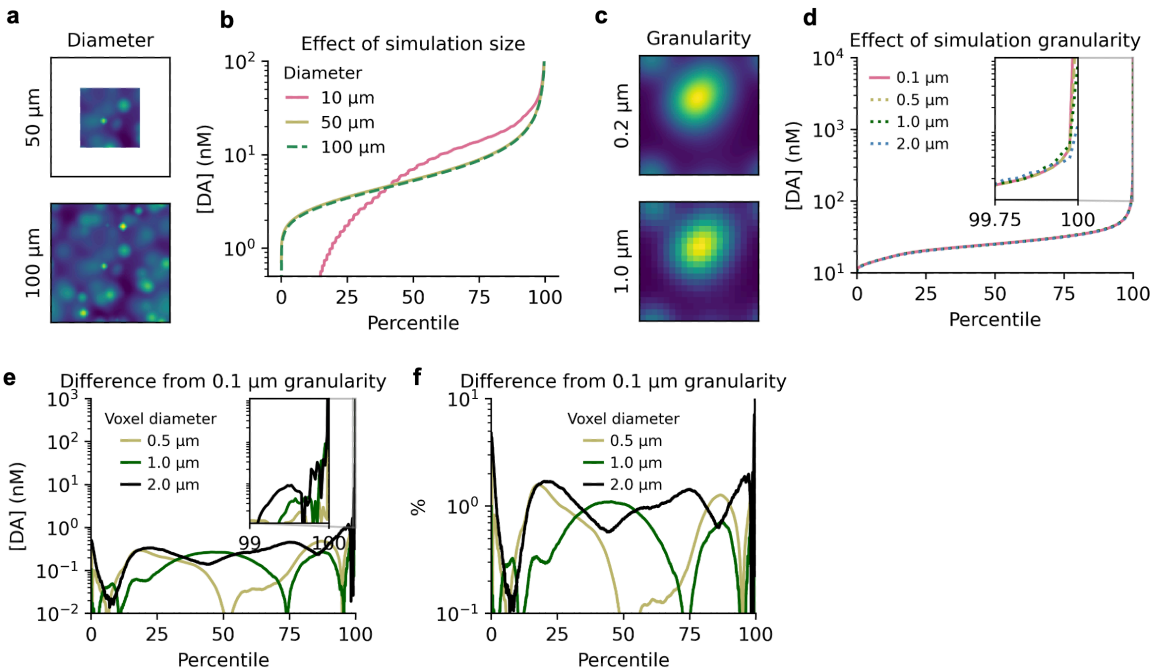

Extended Data Fig. 2 – Simulation size and granularity
a. Schematic of different simulation sizes. **b,** Concentration percentiles at different simulation diameters. Results are not robust until a diameter close to 50 µm is reached (line runs behind 100 µm line). **c,** Schematic of simulation granularity. **d,** Effect of simulation voxel diameter on concentration percentiles. Virtually no difference in concentration profiles below the 99.9th percentile of [DA], with the 1.0 µm voxel size still following 0.1 and 0.5 µm well above that level. Inset shows 99.75th to 100th percentile with y-axis matching main y-axis. **e,** Absolute difference in [DA] between simulations at 0.1 µm voxel diameter and 0.5, 1.0 and 2.0 µm. Inset shows 99th to 100th percentile with y-axis matching main y-axis. **f,** Percentage difference in [DA] between simulations at 0.1 µm voxel diameter and 0.5, 1.0 and 2.0 µm.

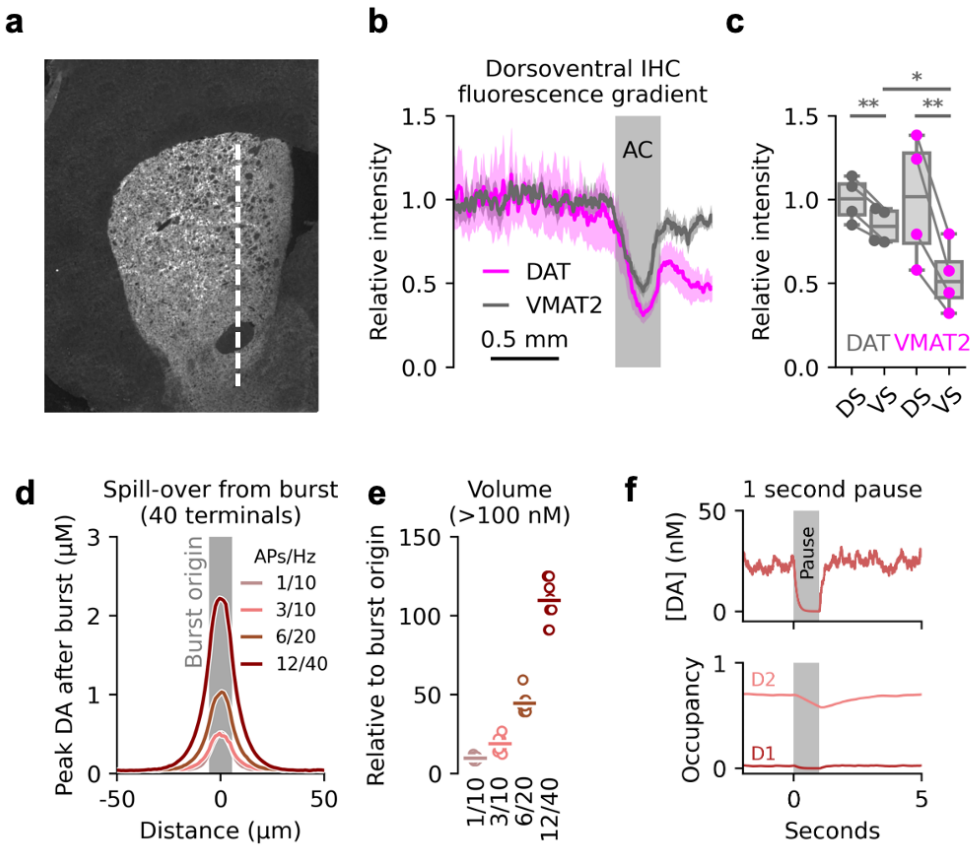

Extended Data Fig. 3 – Histochemical gradient of DAT and VMAT2 fluorescence
a. Representative image of the mouse striatal slices analysed in b. Dashed white line indicates the quantified dorsoventral gradient. **b,** Relative intensity of the DAT and VMAT2 immunosignal in the dorsoventral axis of striatal mouse brain slices from [44]. All slices show a drop at the anterior commissure (AC). Shaded areas around lines denote S.E.M.. **c,** Mean relative intensity of the DAT and VMAT2 signal before and after AC. Two-sided t-test, VS-DAT:VMAT2, P = 0.012(*), n = 4 mice; one-sided t-tests, DAT-DS:VS, P = 0.0021(**), VMAT2-DS:VS, P = 0.0086(**), n = 4 mice. **d,** Peak DA concentration reached at different distances from area with phasic activity for the three firing scenarios in VS. **e,** Volume of space in VS exposed to greater than 100 nM after firing relative to volume of space where terminals actively burst. **f,** Effect of complete pause in firing in VS for 1 second on both average [DA] and D1R and D2R occupation.

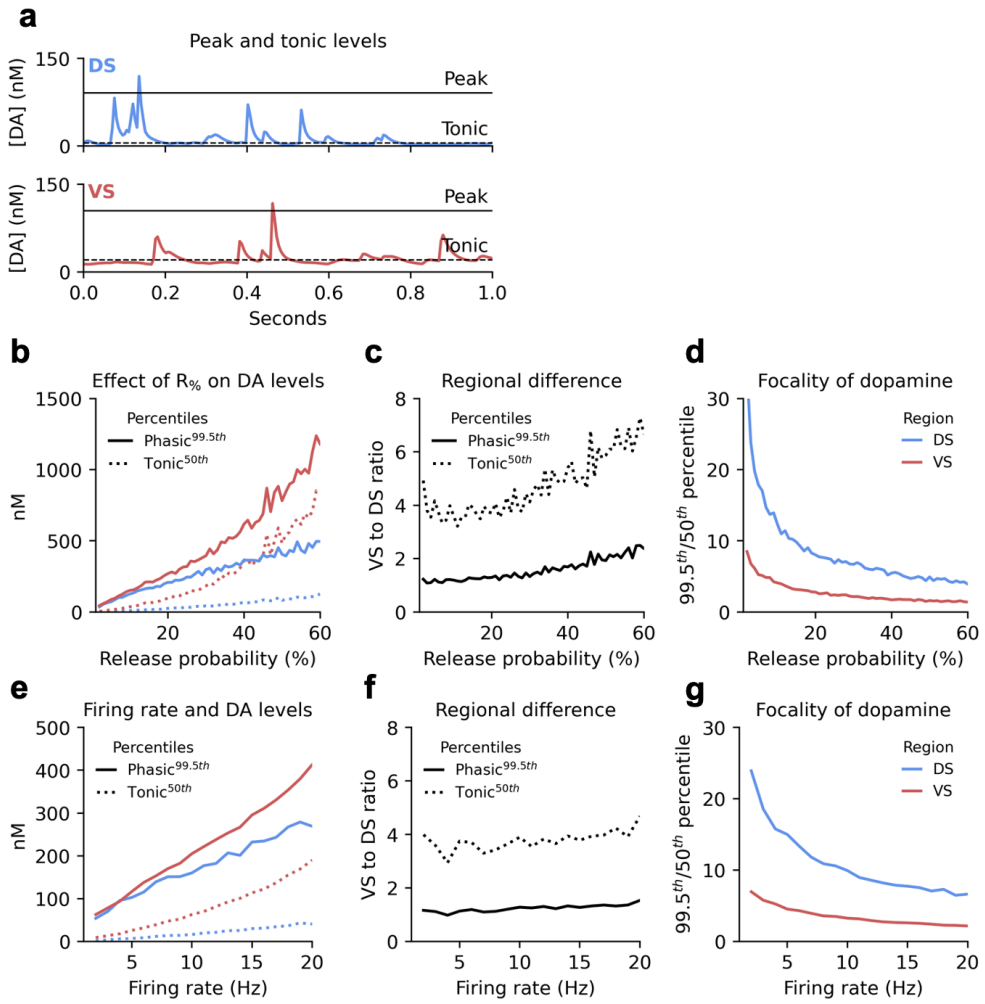

Extended Data Fig. 4 – Model parameter testing

a. Schematic of our definitions of tonic (50th percentile/median, dashed lines) and peak (99.5th percentile, solid line) DA for both the dorsal and ventral striatum. **b,** Effect of changing release probability ($R_{\%}$) on DA concentrations. **c,** Relative difference between the ventral and dorsal striatum at different percentiles for different release probabilities. **d,** Ratio between 99.5th and 50th percentile as a measure of focality for both regions. As $R_{\%}$ increases the concentrations becomes more homogeneous. **e,** Effect of changing firing rate on DA concentrations. **f,** Relative difference between the ventral and dorsal striatum at different percentiles for different firing rates. **g,** Ratio between 99.5th and 50th percentile for both regions. As firing rate increases the concentrations becomes more homogeneous.

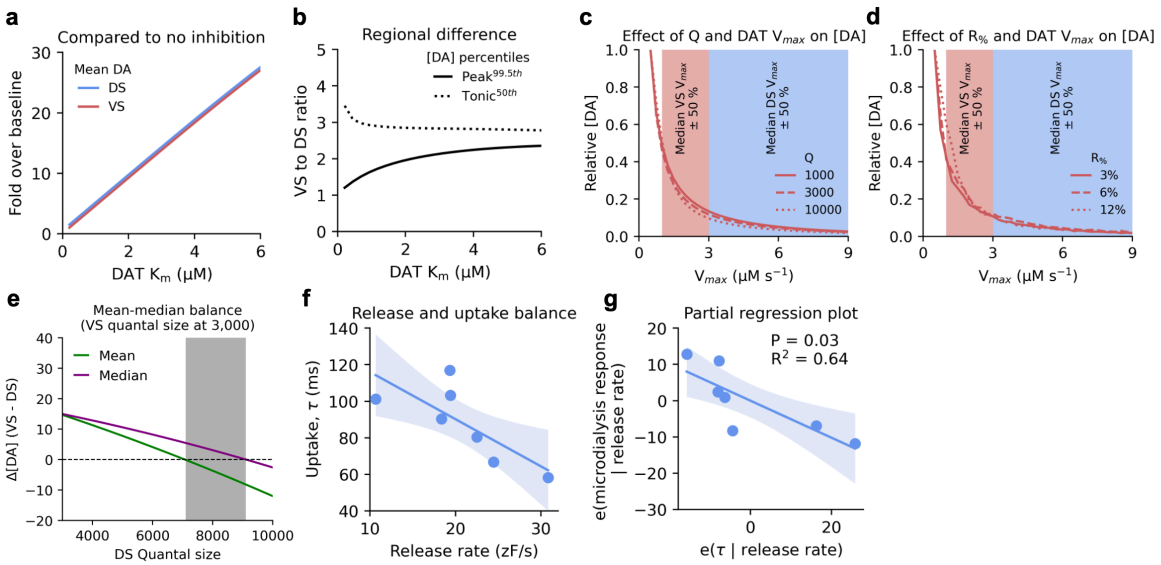

Extended Data Fig. 5 – Fold change during inhibition, V_{max}-sensitivity at different release parameters and release-uptake balance.

a. Fold change over baseline (K_m of 210 nM) for mean DA concentration in the dorsal (DS) and ventral striatum (VS) with changing DAT K_m. **b,** Relative difference between the dorsal and ventral striatum for both phasic and tonic DA at different K_m values. **c,** Effect of changing DAT V_{max} on DA concentrations for three different quantal sizes (Q). [DA] normalized to highest values within each Q. Shaded area indicates median V_{max} for DS and VS as found in the literature shown in Extended Data Table S2 with ± 50%. **d,** Effect of changing DAT V_{max} on DA concentrations for three different release probabilities ($R_{\%}$). [DA] normalized to highest values within each $R_{\%}$. Shaded area indicates median V_{max} for DS and VS as found in the literature shown in Table S2 with ± 50%. **e,** Difference between VS and DS for both mean and median concentrations across different Qs for DS (VS held at 3,000). Shaded area indicates range of Q where median is higher in VS but mean is higher in DS. **f,** Least-square fit linear regression between release rate and autocorrelation decay rate (τ) from (Ejdrup & Wellbourne-Wood et al., 2023[13]). Shaded area highlights 95% C.I. **g,** Partial regression plot (error of the regression in (f) and error between DA response to amphetamine as measured by microdialysis and the release rate from (Ejdrup & Wellbourne-Wood et al., 2023[13]) to show that the less release and uptake correlate, the less release rate can explain the microdialysis response, suggesting release and uptake are partially independent of each other. Shaded area highlights 95% C.I.

Measure	Ratio	DS	VS	Units	Species	Source
TH expression density	100 %	~90	~90	A.U.	Mouse	Alberquilla et al., 2020
TH immunoreactivity	95 %	~68	~64	A.U.	Mouse	Kuroda et al., 2009
TH protein content	150 %	0.07	0.11	ng TH/µg prot.	Mouse	Salvatore et al., 2016
DA content	90 %	~155	~140	ng DA/mg prot.	Mouse	Salvatore et al., 2016
TH immunoreactivity	75 %	2.8	2.1	A.U.	Rat	Huang et al., 2019
TH protein content	66 %	0.36	0.24	ng TH/µg prot.	Mouse	Salvatore et al., 2005
FSCV - $[DA]_p$	91 %	57	52	nM	Rat	May & Wightman, 1989
FSCV - $[DA]_p$	76 %	89.3	67.5	nM	Rat	Garris & Wightman, 1994
Median	90 %	-	-	-	-	-

Extended Data Table 1 – Overview of reports on dopaminergic density and release in the striatum. Only studies that assessed both regions in rodents are included. Studies that stimulate directly in the striatum are omitted due to the large activation of nicotinic receptors on DA terminals [47,89]. A.U. = arbitrary units, DS = dorsal striatum, VS = ventral striatum, TH = tyrosine hydroxylase.

Method	VS/DS Ratio	DS (uM/s)	VS (uM/s)	Species	Source
FSCV	29 %	7.0	2.0	Mouse	Calipari et al, 2012
FSCV	28 %	6.0	1.7	Rat	Calipari et al, 2012
FSCV	47 %	3.0	1.4	Rat	May & Wightman, 1989
FSCV	31 %	6.5	2.0	Mouse	Siciliano et al., 2014
FSCV	44 %	6.0	2.2	Rat	Ferris et al., 2014
Median	31 %	6.0	2.0	-	-

Extended Data Table 2 – Overview of reported V_{max} values for DA uptake in the striatum. Only studies that assessed both regions in rodents are included. DS = dorsal striatum, VS = ventral striatum, FSCV = fast-scan cyclic voltammetry.